Polymer Composites

WILEY | spe INSPIRING PLASTICS PROFESSIONALS

RESEARCH ARTICLE OPEN ACCESS

Sepiolite Nanofibers Decorated With Zn Single Sites: A Sustainable Filler for Mechanically Robust and Self-Healing Ionomeric Elastomer Composites

Paolo Valagussa[1] | Silvia Mostoni[1] | Marianella Hernandez Santana[2] | Itziar Mas Giner[2] | Michele Mauri[1] | Roberto Simonutti[1] | Sandra Diré[3] | Emanuela Callone[3] | Barbara Di Credico[1] | Roberto Scotti[1] | Massimiliano D'Arienzo[1]

[1]Department of Materials Science, INSTM, University of Milano-Bicocca, Milano, Italy | [2]Institute of Polymer Science and Technology (ICTP), CSIC, Madrid, Spain | [3]"Klaus Müller" Magnetic Resonance Lab., Department of Industrial Engineering, University of Trento, Trento, Italy

Correspondence: Silvia Mostoni (silvia.mostoni@unimib.it)

Received: 11 May 2026 | **Revised:** 10 July 2026 | **Accepted:** 19 July 2026

Keywords: filler | rubber nanocomposites | self-healing | sepiolite | ZnO

ABSTRACT

The growing demand for sustainable elastomer management has prompted the development of self-healing cross-linked rubbers. Recent studies showed that adding ZnO to carboxylated nitrile rubber (XNBR) creates thermo-reversible ionic interactions. However, Zn leaching during life cycles of rubber products raises environmental concerns. Moreover, achieving both efficient repairability and high mechanical performances in elastomers remains a major challenge. To address these issues, this work introduces a novel multifunctional filler based on sepiolite nanofibers (Sep) surface decorated with Zn(II) single sites. This is designed to simultaneously provide structural reinforcement, thermally activated self-healing properties and ensure potential reduced metal leaching from XNBR composites. Specifically, naturally occurring Sep was surface functionalized with an amino-substituted silane (APTES) to promote the coordination of Zn(II) centers. Following surface and morphological characterization, Sep@APTES-Zn was incorporated into XNBR to enable the formation of a thermo-reversible ionic network mediated by Zn(II) cations and allow rubber recovery after damage. Indeed, XNBR/Sep@APTES-Zn composites display excellent mechanical properties, remarkable self-repairability and pronounced potential recyclability. Moreover, the structural stability of Zn(II) sites in the materials represents a valuable turning point toward the potential reduction of Zn leaching phenomena. These findings may open new avenues to design and fabricate high-performance and sustainable rubber products with extended service lifetime.

1 | Introduction

The persistent challenges in recycling polymers, particularly elastomers, underscore the urgent need to integrate them into the circular economy, especially given their indispensable role in strategic applications such as rubber products [1, 2]. One potential pathway to achieve this objective is to imbue these materials with self-healing properties [3]. An encouraging possibility is the incorporation of labile bonds into the rubber matrix for imparting both mechanical strength and intrinsic self-repairing ability [4–7]. However, significant issues arise considering the discrepancy between outstanding mechanical properties usually required for rubber-based products, which entail rigid and stable covalently bonded molecular networks, and self-healing, which instead implies polymer chain mobility [8].

In this context, ionomers represent promising materials combining the processability of thermoplastics with the elasticity of rubber [9]. The ionic interactions in ionomers typically arise from electrostatic interactions between anions, such as carboxylates and sulfonates, and cations derived from Groups 1–2, or transition metals [10]. These produce thermo-reversible

Highlights

- Sep@APTES-Zn fillers developed by anchoring Zn(II) single sites on sepiolite nanofibers
- Sep@APTES-Zn filler embedded in XNBR composites creates a thermo-reversible ionic network in the elastomer.
- Synergistic effect ensures high reinforcement and efficient self-healing ability.
- Coordination of Zn(II) on the surface of Sep nanofibers potentially reduces metal leaching.

physical cross-links (i.e., aggregates or ionic clusters), which exert a remarkable influence on the mechanical and physical properties of the polymer and underpins the self-healing behavior [11]. Specifically, the formation of reversible ionic dynamic interactions in rubber matrices via the introduction of ZnO or Zn-based complexes has been recently reported [12]. It was demonstrated that, at a molecular level, Zn^{2+} can form ionic interaction with the carboxylic groups of carboxylated nitrile rubber (XNBR) capable of thermoreversible association. However, the extended use of ZnO or synthetic Zn compounds together with leaching phenomena occurring during the production and life cycle of rubber products, raise potential environmental risks, as ecotoxicity toward aquatic organisms [13, 14]. This creates a paradox: while self-healing capabilities extend the material's lifespan, the environmental impact from its production and eventual disposal may undermine these benefits.

To address these challenges, an increasing attention has been directed toward: (i) the reduction of ZnO utilization in rubber products [15], (ii) the anchoring of Zn-based species onto the filler support, especially Zn centers, through covalent interactions, thus preventing possible metal leaching [16] and (iii) the development of Zn-based self-healing systems that are bio-based and/or biodegradable [16, 17].

As regards ZnO reduction and anchoring, our group has developed novel materials based on ZnO nanoparticles (NPs) [15] or Zn centers [16] directly grown on the surface of silica NPs. These systems act simultaneously as curing activators and reinforcing fillers. The resulting hybrid materials exhibit enhanced curing efficiency and improved dynamic mechanical properties in cured silica/rubber nanocomposites (NCs) compared to those obtained with higher amounts of conventional microcrystalline ZnO [18]. These findings highlight the strong potential of such systems to significantly reduce ZnO usage and Zn leaching in rubber compounding while maintaining or even improving material performance.

The literature also reports several bio-based, Zn-containing self-healing systems across various polymer matrices. For instance, Zhang G. et al. [19] prepared high-performance XNBR NCs by incorporating unmodified lignin and ZnO, able to form metal–ligand coordination bonds with XNBR and the oxygen-containing groups in lignin. The resulting NCs exhibited potentially enhanced recyclability, self-healing capability, and shape-memory properties. Jiang et al. [20] developed instead a flexible lignin-based matrix using a solvent-free, one-pot melt polymerization with thioctic acid and itaconic acid. A rigid dynamic network, formed through the Zn^{2+} coordination with the phenolic hydroxyl/carboxyl groups of lignin, regulates segment motion to impart both mechanical strength and self-healing properties. Recently, reinforced bio-thermoplastic polymers featuring dual healing mechanisms have also been proposed [21]. By blending epoxidized natural rubber with polycaprolactone (PCL) and alginate fillers in the presence of ZnO, the system achieves extrinsic healing via PCL thermal flow and intrinsic healing through alginate-reinforced Zn^{2+} ionic interactions and hydrogen bonding.

The above results indicate that the Zn-ligand coordination is highly effective for balancing mechanical properties and repairability. However, a significant challenge remains in achieving this synergy while preventing environmental metal leaching, particularly relevant to scale up this approach for XNBR NCs. In this context, designing a multifunctional healing agent that integrates structural reinforcement with Zn^{2+} mediated thermoreversible interactions emerges as a captivating strategy. Our recent work validated this approach using alumina NPs decorated with anchored Zn(II) single sites, which significantly improve mechanical reinforcement, thermal conductivity, and self-healing efficiency [22]. Besides, the high structural stability of the anchored Zn(II) sites during curing and processing could effectively suppress zinc leaching, offering a sustainable solution to environmental concerns.

Based on these findings, the present work explores a novel multifunctional filler based on sepiolite (Sep) nanofibers decorated at the surface with Zn single sites to simultaneously maximize reinforcement, deliver thermally activated self-healing properties to XNBR and ensure stable leach-resistant NCs. Among clays, sepiolite has been selected not only for its abundance and low cost but primarily for its unique fibrous architecture, high aspect ratio, and high specific surface area [23]. These features enable exceptional chemical stability and mechanical reinforcement to rubber NCs [24, 25], and provide an ideal platform for functionalization, ensuring a higher degree of filler-matrix interaction in XNBR NCs. In detail, Sep nanofibers were functionalized with an amino-substituted silane (3-aminopropyl-triethoxysilane, APTES) to promote the coordination of Zn(II) single sites via the amino groups. Upon a comprehensive structural, surface, and morphological characterization, the Sep@APTES-Zn filler was incorporated in XNBR NCs, and the formation of thermally reversible ionic cross-links between Zn^{2+} and the carboxylate pendant groups of XNBR investigated as a route to rubber recovery after damage. The results of this study may open new avenues to design and fabricate high-performance and sustainable rubber products with extended lifetime, with paramount fallouts for automotive and rubber components industries.

2 | Experimental Section

2.1 | Materials

Synthesis of Sep@APTES-Zn: sepiolite (Sep) Pangel S9 was supplied by Tolsa and extracted from the landfill of Vallecas (Spain); (3-aminopropyl)-triethoxysilane ($H_2N(CH_2)_3Si(OC_2H_5)_3$,

APTES, 99%), sodium hydroxide pellets (NaOH) and ammonium hydroxide (NH_4OH, 25%) were purchased from Merck Life Science; zinc nitrate hexahydrate ($Zn(NO_3)_2$ $6H_2O$, 99%) was purchased from Alfa Aesar, and absolute ethanol (EtOH, 99.8%) was purchased from Exacta Labcenter.

Preparation of rubber NCs: carboxylated nitrile rubber (XNBR, KRYNAC X 750, 27 wt % acrylonitrile content and 7 wt% carboxyl groups) was provided by Arlanxeo. Zinc oxide (ZnO) as a cross-linking agent and toluene (≥99.9%) were supplied from Merck Life Science. Stearic acid (SA, >98.5%) to investigate the Zn(II) coordination of Sep@APTES-Zn with carboxylic groups was purchased from Merck Life Science.

2.2 | Synthesis of Sep@APTES-Zn

The preparation of Sep@APTES-Zn was adapted from a two-step procedure previously developed to anchor Zn(II) single sites on the surface of SiO_2 and Al_2O_3 NPs [16, 22]. For SepS9, an additional washing step was added to remove any impurities and promote its surface reactivity, by treating 10.0 g of SepS9 with 500 mL of a NaOH solution 0.01 M under stirring for 24 h at room temperature (RT). The powder was then recovered by centrifugation (9000 rpm, 20 min), washed with distilled water until neutral pH and dried overnight in a vacuum oven (75°C, 15 mbar) on a Petri dish. The obtained sample was labeled as Sep-OH and used as a substrate for Zn(II) anchoring procedure. To this purpose, Sep-OH was surface functionalized through the hydrolysis and condensation of APTES (step I, Scheme 1). 1.0 g of Sep-OH was dispersed in 30 mL of EtOH at reflux under stirring with 160 μL of NH_4OH and after 10 min 1.15 mL of APTES was added, corresponding to a molar ratio between APTES: surface hydroxyl group of Sep-OH (n_{APTES}:n_{OH}) of 1:2. The amount of surface silanols of Sep-OH was determined by thermogravimetric analysis (TGA) according to Equations S1,S2 and was equal to 9.6 mmol g^{-1}. After 24 h, the product, denoted as Sep@APTES, was centrifuged (9000 rpm, 20 min), washed twice with EtOH and dried overnight (75°C, 15 mbar). Subsequently, Zn(II) centers were anchored to the surface of Sep@APTES through its coordination with the terminal —NH_2 groups of APTES (step II, Scheme 1). To a dispersion of 1.0 g of Sep@APTES in 50 mL of EtOH heated at reflux, 0.267 g of $Zn(NO_3)_2{\cdot}6H_2O$ was added, corresponding to a Zn: APTES molar ratio (n_{Zn}:n_A) equal to 1:2. The amount of APTES was determined according to TGA (Equation S3-S4) The reaction was carried out for 2 h at reflux and the product isolated by centrifugation (9000 rpm, 20 min), washed twice with EtOH and dried overnight (75°C, 15 mbar). This material was labeled Sep@APTES-Zn. The whole synthetic process was scaled up to 50 g of Sep@APTES-Zn.

2.3 | Characterization of Sep@APTES-Zn

Both Sep@APTES and Sep@APTES-Zn were then fully characterized to confirm the effective functionalization with APTES and anchoring of surface Zn(II) centers. Powder X-ray diffraction (P-XRD) patterns were collected using a Rigaku Miniflex 600 diffractometer (Cu Kα incident beam, Cu Kα1 $\lambda = 1.5406$ Å, Kα2 $\lambda = 1.54433$ Å), in the range of 2θ between 5° and 90° (2θ step size of 0.020°, scan rate of 1 min^{-1}). Nitrogen physisorption measurements were carried out using the Autosorb-IQ-C-MP AsiQwin, applying the BET method for data elaboration. Prior to analysis, a degassing step was performed at 80°C for 24 h to remove surface contaminants and adsorbed gases. Infrared spectroscopy in Attenuated total reflectance mode (ATR-FTIR) spectra were recorded by using a Nicolet iS20 FTIR spectrometer (4 cm^{-1} resolution, 550–4000 cm^{-1} range, 32 scans).

Solid-state magic-angle spinning nuclear magnetic resonance (MAS-NMR) measurements were conducted on a Bruker 400WB spectrometer equipped with a CPMAS dual-band probe. Spectra were acquired with cross polarization (CP) under the following conditions: ^{13}C frequency: 100.48 MHz, contact time 2 ms, decoupling length 6.8 μs, recycle delay: 3 s, 8 k scans. ^{29}Si frequency: 79.48 MHz, contact time 5 ms, decoupling length 6.8 μs, recycle delay: 8 s, 1.6 k scans. Samples were packed in 4 mm zirconia rotors, which were spun at 7 kHz under air flow. Adamantane and Q_8M_8 were used as external secondary references. According to the ^{29}Si NMR notation, the Si species are labeled Tn and Qn indicating R-SiO3 and SiO4 structural units, respectively, and n is the number of bridging oxygens.

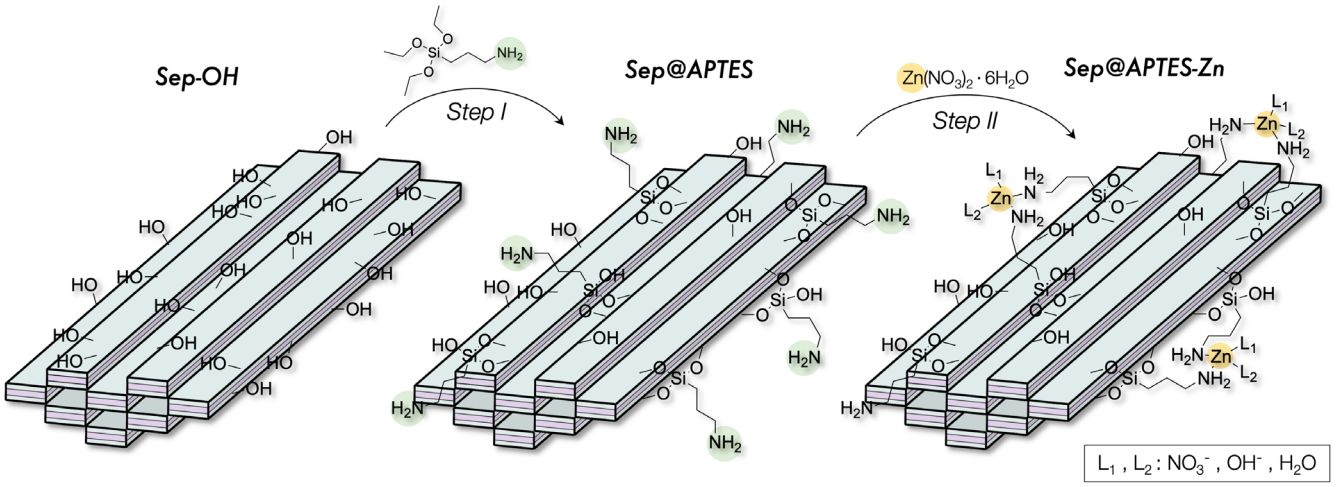

SCHEME 1 | Reaction pathway for the surface functionalization of Sep fibers with Zn(II) single sites. L_1 and L_2 shown in Sep@APTES-Zn represent possible groups coordinated to Zn(II), as NO_3^- or OH^-.

The quantity of grafted APTES in Sep@APTES was assessed through a TGA using a TGA2 STARe system and calculated according to Equation S3,S4. The analysis was conducted within a temperature range of 30°C–1000°C, a heating rate of 10°C min^{-1}, and constant air flow of 50 mL min^{-1}. An isothermal step at 150°C for 10 min was employed to ensure complete weight loss related to physisorbed solvents and water molecules. The Zn amount in Sep@APTES-Zn was measured by inductively coupled plasma–optical emission spectrometry (ICP-OES) using an ICP-OES Optima 7000 DV instrument (PerkinElmer). The solid sample (0.20 g) was dissolved in 4 mL of HNO_3 and 4 mL of HCl and then mineralized in a microwave Milestone Ethos mineralizer (8 min at 1000 W and 160°C, 5 min at 1000 W and 200°C, 20 min at 1000 W and 200°C). The solution was diluted with 12 mL of Milli-Q water and then 1:2 with Milli-Q water.

The morphology was analyzed using scanning electron microscopy (SEM) with a Zeiss Gemini 500 microscope (accelerating voltage of 5.0 kV, in-lens detector) equipped with a field emission gun (FEG) and a Bruker Quantax EDS system for elemental composition analysis. Powdered samples were mounted on a metallic sample holder with conductive carbon tape and subsequently coated with a thin layer of gold by sputter coating using a VPI SD-900C device. Transmission electron microscopy (HR-TEM) analyses were conducted with a Jeol-JEM 2100 Plus instrument (accelerating voltage of 200 kV) equipped with an 8-megapixel Gatan Rio camera. The instrument includes an Oxford NanoAnalysis energy dispersive X-ray system (EDX) for compositional mapping. The samples were deposited by drop-casting of NPs dispersion in EtOH (500 ppm) onto a carbon coated copper mesh grid.

Electron paramagnetic resonance (EPR) measurements were carried out on Sep@APTES-Zn/Cu, prepared by replacing a small amount of $Zn(NO_3)_2{\cdot}6H_2O$ with $Cu(NO_3)_2{\cdot}3H_2O$ to obtain Cu(II) coordinated centers on Sep as a paramagnetic probe (Cu:Zn molar ratio 1:100). The EPR spectra were acquired at 130 K using a Bruker EMX spectrometer operating at X-band frequency and equipped with an Oxford cryostat.

2.4 | Sep@APTES-Zn Interaction With Stearic Acid as a Model Compound

To preliminarily investigate the coordination of Zn(II) in Sep@APTES-Zn with the carboxylate groups of XNBR, Sep@APTES-Zn was mechanically mixed with SA as a model compound, using a SA:Zn molar ratio equal to 4:1 to ensure an excess of SA. The mixtures were analyzed by differential scanning calorimetry (DSC) analysis to check the formation and the nature of Zn(II)-stearic acid complexes, according to our previous studies [22]. The experimental conditions are reported in the Supporting Information.

2.5 | Preparation and Characterization of XNBR NCs

XNBR/Sep NCs were fabricated by mixing XNBR, Sep-based filler and ZnO as a curing agent with a water-cooled two-roll mill (MGN-300S, Comerio Ercole S.P.A.). Initially, 100 g of XNBR underwent mastication for 5 min to enhance its processability. Then, three different amounts of bare Sep-OH or Sep@APTES-Zn (5, 10, and 15 parts per hundred, phr) were progressively incorporated into the rubber matrix. Lastly, suitable amounts of ZnO were added to achieve a total Zn content of 8 phr (Table 1). The overall mixing duration ranged between 30 and 40 min, depending on the filler content to ensure thorough dispersion and homogenization. The NCs were identified respectively as XNBR/Sep-X and XNBR/Sep@APTES-Zn-X, where X denotes the filler loadings. A reference compound was prepared at equal Zn content by mixing 100 g of XNBR and 10 g of ZnO, labeled as XNBR.

To further discriminate the influence of Zn(II) single sites on the functional properties of the material, an additional compound was prepared using Sep@ZnO as a filler. In this system, ZnO NPs were previously grown on the surface of Sep-OH fibers. This filler was synthesized according to the experimental procedure reported in the Supprting Information and previously adopted for other silica-based materials [16]. In this case, only

TABLE 1 | Amounts used for the preparation of XNBR NCs expressed in parts per hundred rubber (phr).

Formulation	Rubber XNBR	Curing agent ZnO	Sep-OH	Sep@APTES-Zn	Sep@ZnO
XNBR	100	10	—	—	—
XNBR/Sep-5	100	10	5	—	—
XNBR/Sep-10	100	10	10	—	—
XNBR/Sep-15	100	10	15	—	—
XNBR/Sep@APTES-Zn-5	100	9.8	—	5	—
XNBR/Sep@APTES-Zn-10	100	9.6	—	10	—
XNBR/Sep@APTES-Zn-15	100	9.4	—	15	—
XNBR/Sep@ZnO-10	100	9.6	—	—	10
XNBR/Sep@APTES_N	100	—	10	—	—
XNBR/Sep@APTES-Zn_N	100	—	—	10	—
XNBR/Sep@ZnO_N	100	—	—	—	10

one filler content equal to 10 phr was tested, corresponding to a Zn content of 8 phr, and the resulting compound labeled as XNBR/Sep@ZnO-10.

Moreover, in order to gain deeper insight into the microscale interactions between Zn centers and rubber chains, three ad hoc formulations were prepared labeled as XNBR/filler_N. These systems contain 10 phr of different sepiolite-based fillers, namely Sep@APTES, Sep@APTES–Zn and Sep@ZnO, whereas ZnO was intentionally excluded to isolate and better evaluate the specific role of the zinc species anchored on the filler surface and their potential interactions with the rubber matrix.

The vulcanization process of XNBR NCs was carried out by compression molding ($T = 160$°C, $p = 180$ bar) using a hydraulic press (TP300, Gumix). The curing time was optimized based on the rheometric curing curves and particularly based on the time corresponding to 90% of the maximum torque (t_{90}). The final specimens were cut for the characterization tests with a P-VS 3000 universal sample cutter (MonTech) operating at an 8 kN force. The curing curves were registered using an oscillating disk rheometer (RPA 2000, Alpha Technologies), operating at a 0.5° oscillation amplitude and 1.7 Hz frequency for 60 min at 160°C.

The NCs were characterized through ATR-FTIR in the wavenumber range of 550–4000 cm^{-1} (resolution of 4 cm^{-1}, 64 scans). Their thermal stability was assessed via TGA, by heating from RT to 600°C in N_2 atmosphere (50 mL min^{-1}), and then up to 800°C in air (50 mL min^{-1}), with a heating rate of 10°C min^{-1}. The tensile properties of the vulcanized NCs were measured on dumbbell-shaped specimens (initial gauge length of 35 mm) using an Instron universal testing machine (model 2204) equipped with a 50 kN load cell and at a constant crosshead speed of 200 mm min^{-1}. The stress values were recorded at increasing strain levels, namely 100% (M100), 300% (M300), and 500% (M500), along with the tensile strength (TS) and elongation at break (EB), corresponding to the maximum stress and strain observed at the breaking point, respectively. The reported values were calculated as the medium value of five independent measurements. The dynamic mechanical behavior was investigated using a DMA Q800 analyzer (TA Instruments, New Castle, DE, USA), under tension mode, in the temperature range from −100°C to 150°C, using the following parameters: displacement amplitude = 15 μm, frequency = 1 Hz, heating rate = 2°C min^{-1}.

The ^{1}H Time Domain Nuclear Magnetic Resonance (TD-NMR) analyses of the NCs were carried out using a Bruker Minispec instrument, a time-domain NMR spectrometer equipped with a permanent magnet that produces a magnetic field of 0.47 T and a Larmor frequency of 20 MHz for ^{1}H nuclei.

2.6 | Self-Healing Properties of XNBR NCs

Healing tests were carried out based on the implemented protocol reported in our previous work [16] and optimized for XNBR-based systems [26]. To this purpose, rectangular samples (dimension of 10.5 × 1 cm, thickness of 2 mm) were cleanly cut in half and subsequently repositioned in direct contact within a mold featuring rectangular cavities that matched the sample dimensions. Then, the samples were subjected to a pressure of 180 bar for 3 h using a hydraulic press set at 110°C (Scheme 2).

Finally, the healing efficiency (η) was assessed by comparing the mechanical properties of the repaired samples with those of the pristine ones, subjected to the same temperature and pressure conditions of the healed NCs. Specifically, the values of TS and EB measured before and after the healing procedure were used in the following equations to calculate η:

$$\eta\,(\%) = \frac{TS_{healed}}{TS_{pristine}} \times 100 \quad (1)$$

$$\eta\,(\%) = \frac{EB_{healed}}{EB_{pristine}} \times 100 \quad (2)$$

3 | Results and Discussion

3.1 | Characterization of Sepiolite-Based Fillers

The structural features of Sep-OH, Sep@APTES and Sep@APTES-Zn were first investigated by P-XRD. The XRD pattern of Sep-OH (Figure S1) shows the characteristic peaks of crystalline Sep (JCPDS 01–075-1597). In particular, the intense peak at $2\theta = 7.3°$, as well as additional reflections at $2\theta = 12.3°$, 17.7°, 19.8°, and 35.0°, correspond to the (110), (130), (150), (060), and (371) planes, respectively, and are typical of layered minerals. The same diffraction peaks remain unaltered in Sep@APTES and Sep@APTES-Zn, indicating that the crystalline structure is preserved following surface functionalization with APTES and Zn.

The porosity and surface area values were then evaluated by nitrogen physisorption experiments. The nitrogen adsorption–desorption isotherm of Sep-OH shows a combination of type I and

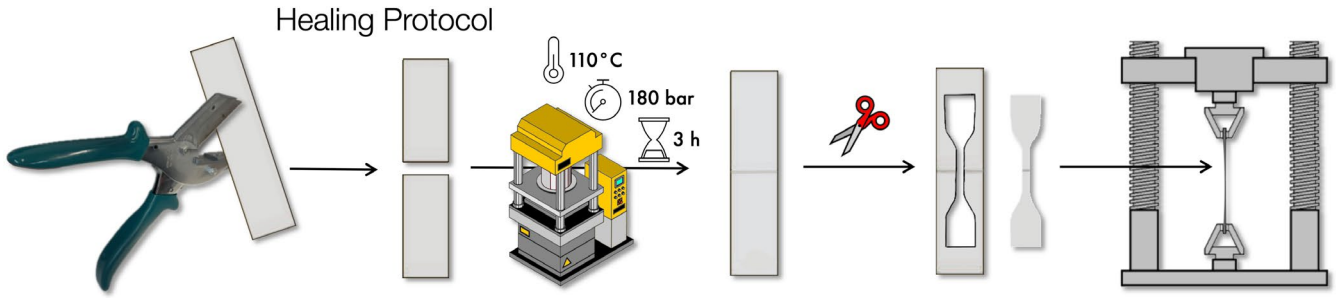

SCHEME 2 | Protocol utilized for the determination of the healing efficiency.

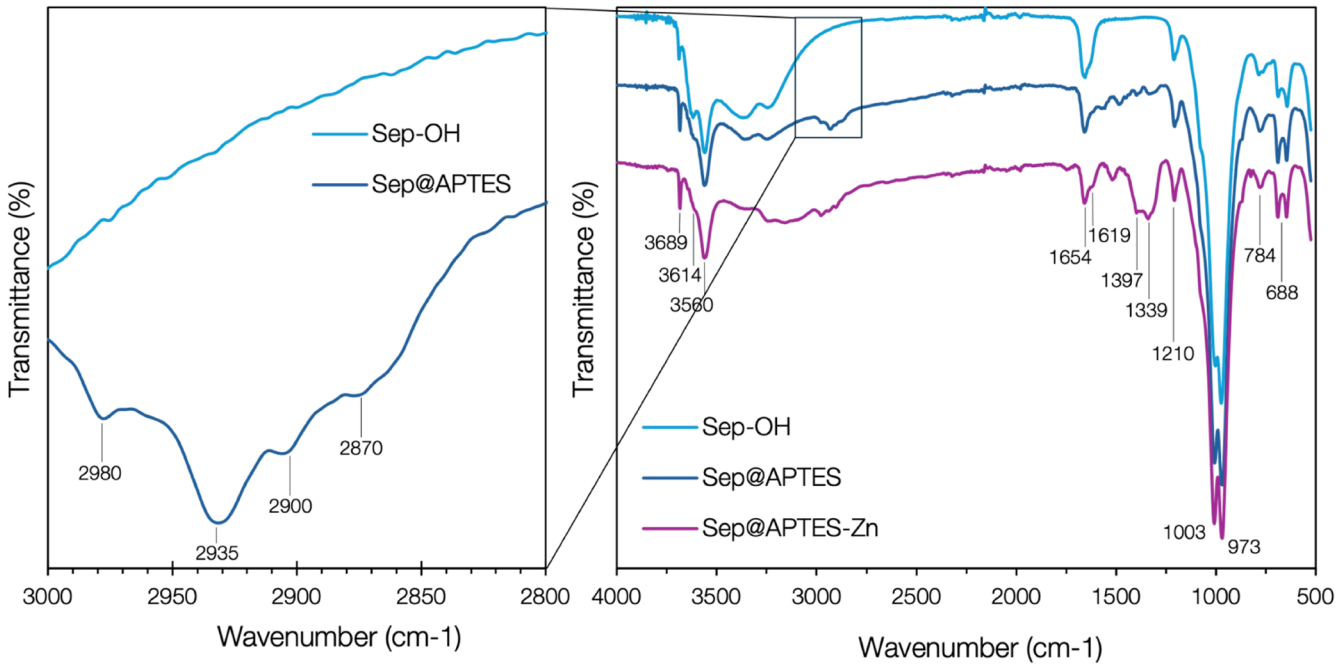

FIGURE 1 | FTIR spectra of Sep@APTES and Sep@APTES-Zn in comparison to Sep-OH fibers. Left side: Magnifications of the spectral regions 3000–2800 cm^{-1}.

IV isotherms according to IUPAC classification (Figure S2a), where the mesoporous component arises due to the aggregation of Sep nanofiber that generates interparticle voids. The resulting specific surface area (SSA_{BET}) of Sep-OH is $259 \pm 1\ m^2\ g^{-1}$, mainly divided into two contributions, that is, an external surface area equal to $149\ m^2\ g^{-1}$ and a micropore-associated area of $109\ m^2\ g^{-1}$, with a total pore volume of $0.262\ cc\ g^{-1}$. The measured isotherms of both Sep@APTES and Sep@APTES-Zn exhibit only a very slight hysteresis (Figure S2b,c), indicating only a residual micropore filling occurring. Moreover, the decrease in the external surface area to $46 \pm 1\ m^2\ g^{-1}$ for Sep@APTES and to $44 \pm 1\ m^2\ g^{-1}$ for Sep@APTES-Zn can be attributed mainly to pore occlusion resulting from surface functionalization.

The FTIR spectra of Sep-OH, Sep@APTES, and Sep@APTES-Zn are reported in Figure 1. In all spectra, the typical peaks of bare Sep due to the stretching vibrations of OH groups bound to Mg in the octahedral layers are observed in the 3550–3700 cm^{-1} region, the Mg—O—H bending at 688 cm^{-1}, and the coordinated/adsorbed water of magnesium at 1619 and 1654 cm^{-1}. Besides, the peaks at 973, 1003, and 1210 cm^{-1} are related to the stretching of Si—OH and Si—O—Si groups in the tetrahedral layers, respectively, whereas the Si—O—Si bending mode is observed at 784 cm^{-1}. The functionalization with APTES in Sep@APTES is suggested by the appearance of peaks in the region at 2940–2860 cm^{-1} (see magnification in the left side of Figure 1), assigned to the asymmetric and symmetric stretching vibrations of —CH_2 groups in the alkyl chains of APTES, reported as reference in Figure S3. Besides, a reduction of the intensity of FTIR peaks due to —OH groups and adsorbed water compared to Sep-OH suggests the partial consumption of surface hydroxyl groups and the surface modification occurring due to APTES condensation over silica. After the Zn addition, the appearance of the two peaks at 1397 cm^{-1} and 1339 cm^{-1} may be connected to residual nitrate groups due to the zinc precursor (Figure S3).

SS-NMR analyses confirm the functionalization of Sep@APTES and Sep@APTES-Zn. In the ^{13}C CPMAS NMR spectrum of Sep@APTES, the three resonances at 10, 22, and 42 ppm are assigned to the methylene carbons (1, 2, and 3) of APTES propyl chain (Figure 2), thus proving the presence of the grafted silane on the clay surface. The chemical shift of C1 (10 ppm) indicates the silane condensation, which is probably not complete considering the signals at 18 and 60 ppm, attributable to residual non-hydrolysed ethoxy groups or ethanol. The broadening of carbon 2 resonance arises from the presence of two overlapped components due to chain folding, thereby producing two types of terminal amino groups [27, 28]. Accordingly, the components at 26 and 22 ppm can be associated with propyl chains bearing free terminal —NH_2 and —NH— groups, respectively. The presence of —NH— groups is related to the high reactivity of amino groups toward environmental CO_2, as evidenced by the carbonyl resonance observed at 163 ppm [29]. Interestingly, the methylene signals undergo further modification following the addition of Zn(II) ions in Sep@APTES-Zn. In particular, the C2 downfield component attributed to free —NH_2 almost disappears in favor of the signal at 22 ppm, which is known to be highly sensitive to terminal —NH— environments, strongly suggesting zinc coordination (it is worth to mention that the C=O signal disappeared). Moreover, all the carbon resonances become sharper compared to those of Sep@APTES, indicating a more ordered arrangement of the grafted chains.

Additionally, by comparing the ^{29}Si CPMAS NMR spectra of Sep@APTES and Sep-OH (Figure S4), both the appearance of T^3 and T^2 resonances at 65 and 56 ppm, together with the decrease in intensity of the Q^2 resonance and the small downfield shift of Si1 Q^3 peak belonging to sepiolite [30] in the spectrum of Sep@APTES clearly indicate the successful functionalization. In agreement with the trends noticed in the ^{13}C spectra, T resonances become sharper and more resolved in the silicon

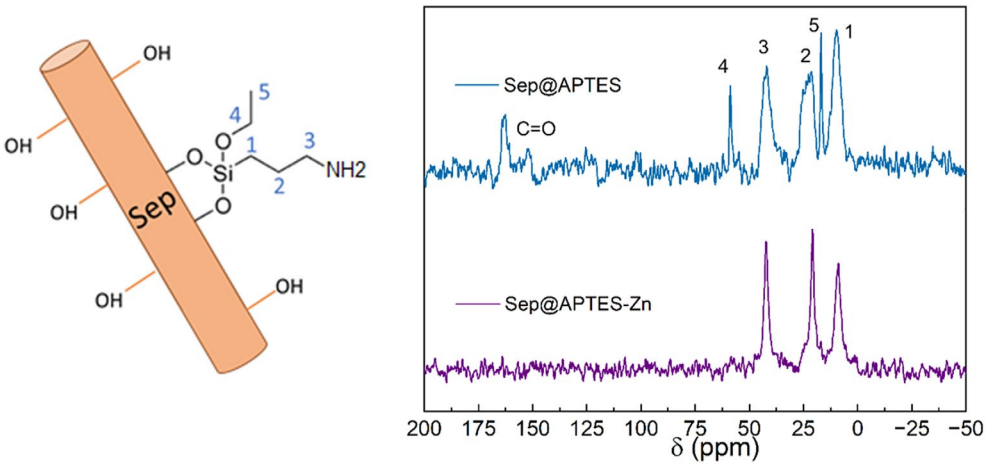

FIGURE 2 | ^{13}C CPMAS NMR spectra of Sep@APTES and Sep@APTES-Zn filler; a graphical representation of Sep@APTES is shown in the inset, along with the numbering of APTES carbon atoms.

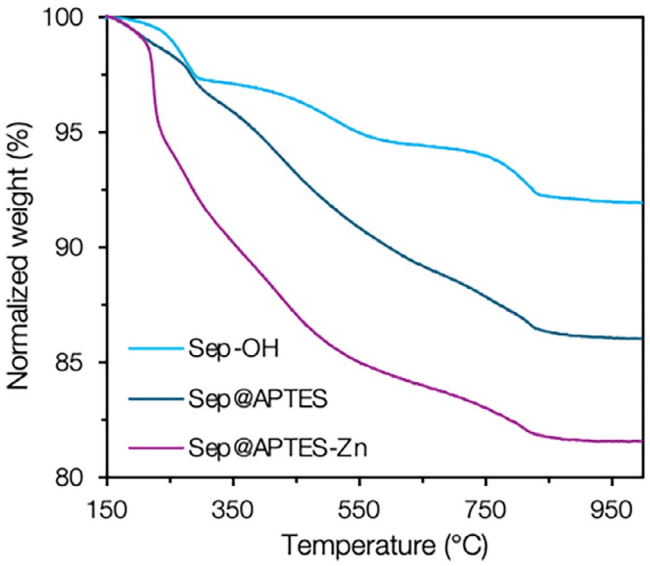

FIGURE 3 | TGA thermal profiles of Sep@APTES and Sep@APTES-Zn compared to bare Sep-OH.

spectrum of Sep@APTES-Zn; moreover, a small upfield shift of S1 Q^3 peak could indicate rearrangement of Sep channels to accommodate the filler [31].

The amount of APTES grafted onto Sep@APTES surface was quantified by TGA analysis by the weight loss percentage measured between 150°C and 1000°C. The thermal degradation profile of Sep@APTES shows a strong increase in the weight loss compared to Sep-OH (Figure 3), ascribable to the presence of additional organic units due to APTES. Thus, the total amount of APTES, expressed as weight percentage (w_{AP}, %) was calculated according to Equation S4 and is equal to 9.5 wt%. In addition, from a comparison of Sep@APTES-Zn thermogram with that of Sep@APTES, a more pronounced weight loss around 250°C is observed. According to Reddy et al. [32], this feature may be attributed to the thermal decomposition of the amine–Zn(II) complex anchored on the Sep surface, supporting the Zn(II) anchoring over sepiolite through the amino groups, as already pointed out by ^{13}C-NMR results.

The morphology of sepiolite-based materials was then investigated by means of SEM and TEM microscopies. SEM images of Sep@APTES-Zn (Figure S5) acquired at two different magnifications highlight the characteristic fibrous morphology of the phyllosilicate, with interconnected fibers forming bundle-like aggregates, observed also in bare Sep-OH (data not reported).

Similarly, TEM micrographs exhibit a needle-like morphology with diameters of 40–70 nm and lengths of 0.5–2 μm in all samples. More interestingly, the coupled TEM-EDX elemental maps acquired on Sep@APTES-Zn (Figure 4) confirm the presence of Si, Mg, and O as the major constituents of the fibers, as well as the presence of Zn, which is homogeneously distributed and well localized on the surface of sepiolite fibers. Moreover, the amount of Zn(II) in Sep@APTES-Zn, as determined by ICP-OES, was found to be 3.20 wt%, thus confirming the successful zinc anchoring close to the nominal values.

To assess the ability of APTES amino groups to coordinate single metal centers at the surface of Sep, EPR analysis was performed on Sep@APTES-Zn/Cu, on an ad hoc sample where Cu(II) was introduced as a paramagnetic probe by replacing a small fraction of Zn(II). The EPR spectrum (Figure S6) shows resonance lines attributable to a monomeric Cu(II) species with axial symmetry ($g\| = 2.26$, $g\perp = 2.06$, $A\| = 168.9 \times 10^{-4}\,cm^{-1}$). The magnetic tensor values are consistent with elongated tetragonal, square planar, or square pyramidal geometries featuring two nitrogen and two equatorial oxygen ligands (see inset in Figure S6) [33]. These results indicate that isolated Cu(II) anchored to sepiolite are coordinated by two APTES ligands, while the equatorial oxygen donors may arise from water molecules, hydroxyl groups, or nitrates. Even though this is indirect information on the APTES ligands, it confirms that APTES is available for the metal coordination and may coordinate Zn(II) centers over the surface of Sep as well, as previously observed with NMR and TGA analyses.

In summary, the characterization of Sep@APTES-Zn demonstrates that Zn(II) has been successfully anchored to the Sep surface through coordination of amine groups of APTES, giving rise to a Zn chemical environment as possibly depicted in Scheme 1. This is also in agreement with our previous works

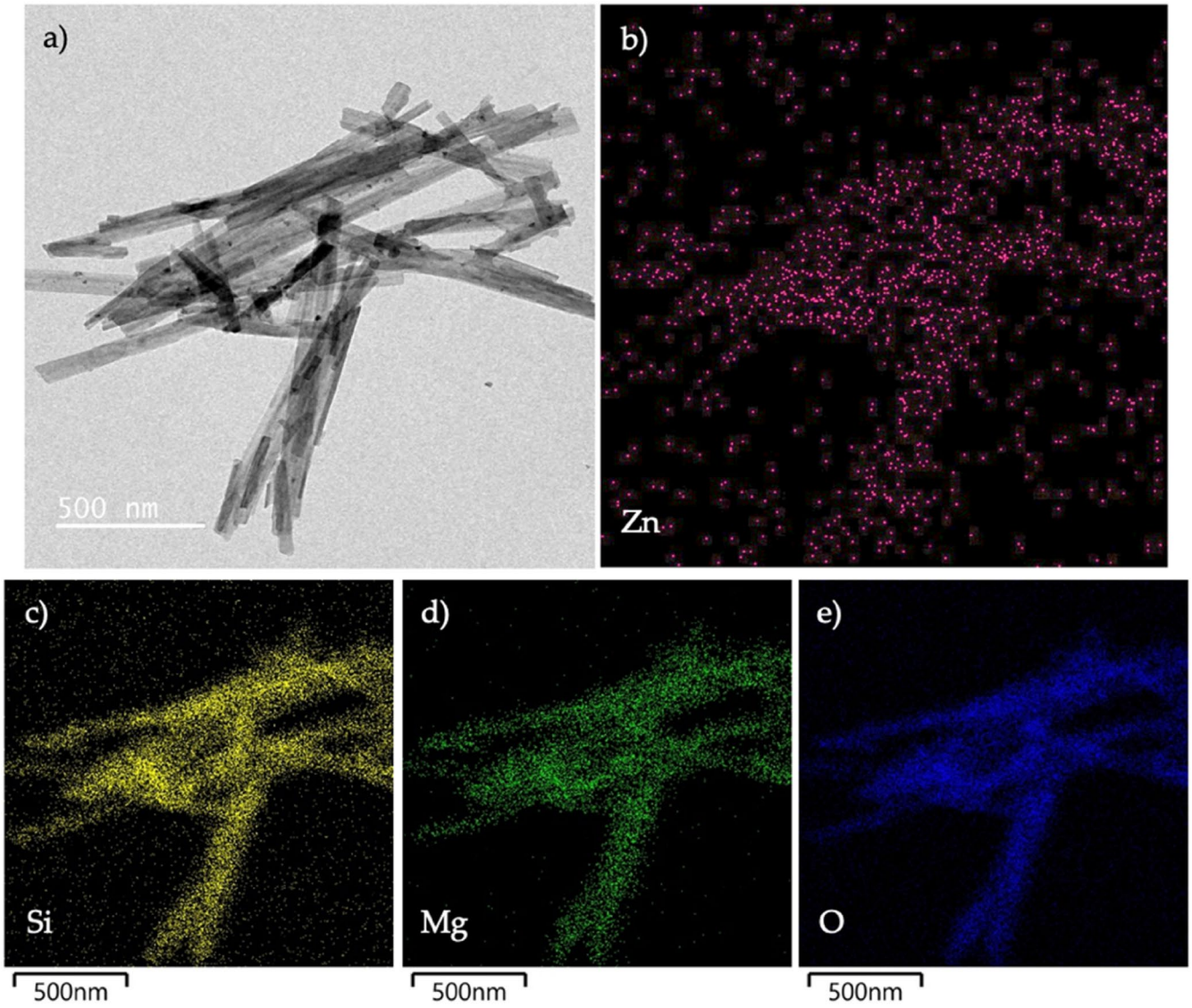

FIGURE 4 | TEM image of Sep@APTES-Zn (a) and corresponding EDX elemental maps collected on the sample for Zn (b), Si (c), Mg (d), O (e).

where Zn(II) centers were anchored on silica and alumina NPs. In this conformation, Zn centers are potentially exploitable for the coordination with the carboxyl groups of XNBR, promoting the formation of ionic interactions capable of enabling thermoreversible association.

3.2 | Characterization of XNBR NCs

XNBR NCs were prepared using Sep@APTES-Zn as a multifunctional filler. In this system, the functionalized Sep acts both as a reinforcing filler and as a source of coordination sites for the carboxylate end groups of the polymer chains, promoting ionic cross-linking during curing. The structural, mechanical, and morphological properties of the resulting NCs were investigated to elucidate the role of the filler within the elastomeric matrix and its impact on the overall material performance.

The good incorporation of the filler within XNBR was first assessed by performing TGA analysis on the cured NCs (Figure S7). All NCs show a major weight loss starting at around 350°C due to XNBR degradation, even though XNBR-Sep-X and XNBR-Sep@APTES-Zn-X NCs are characterized by a slight increase in the thermal stability compared to bare XNBR, due to the filler introduction. Furthermore, the distinct increase in the residual mass fraction at 800°C observed with higher filler loadings reflects the progressively greater amounts of filler incorporated during preparation and aligns closely with their nominal values.

FTIR analysis of filled XNBR NCs was performed to gain insights into the rubber compounds' chemical structure. Figure 5 summarizes the ATR-FTIR spectra recorded for pristine uncured XNBR and XNBR/Sep-APTES-Zn-10 NC representative sample before and after curing.

In details, XNBR (Figure 5, left side) is characterized by two peaks at 2922 cm^{-1} and 2848 cm^{-1}, corresponding to the asymmetric and symmetric stretching of —CH_2 groups in the polymer backbone; a peak at 2238 cm^{-1}, associated with the stretching vibration of the nitrile triple bond —C≡N; peaks at 1640–1670 cm^{-1} and at 1439 cm^{-1}, related to C═C stretching modes

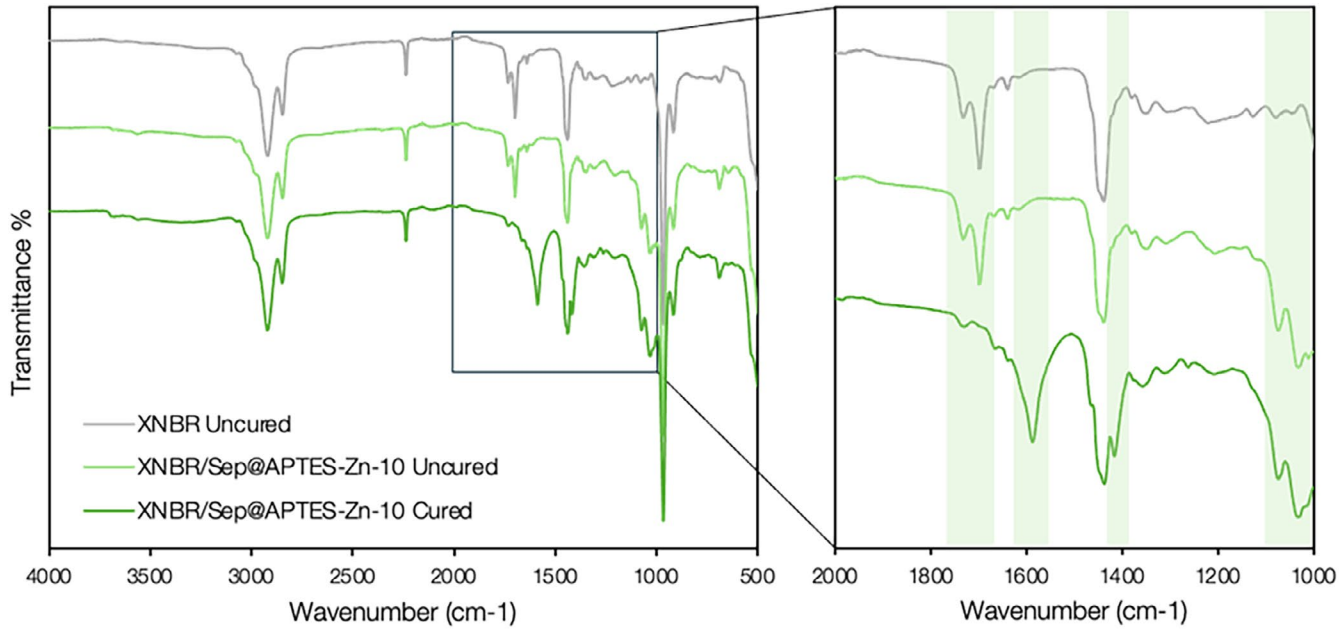

FIGURE 5 | On the left: FTIR spectra of XNBR/Sep@APTES-Zn-10 as a representative sample before and after the curing process in comparison to the uncured XNBR NC. On the right: Magnification of the 1000–2000 cm^{-1} spectral region. Shaded areas highlight the main absorption bands connected to the Zn(II) coordination to carboxylate groups of XNBR.

and to the in-plane —CH deformation of methylene groups, respectively. Moreover, the peaks at 1733 cm^{-1} and 1699 cm^{-1} correspond to the stretching of the carboxylic groups (—COOH) and their respective hydrogen-bonded form. These two peaks are visible in both the uncured NCs (Figure 5, right side) but tend to disappear in the cured compounds and are replaced by two distinct peaks at 1587 cm^{-1} and 1415 cm^{-1}. This behavior is detected both in the cured XNBR (data not reported) and in the XNBR/Sep@APTES-Zn-X NCs. The latter two peaks are typical of Zn-carboxylate complexes with a unidentate coordination [34, 35] and thus represent direct evidence of the ionic interactions between —COO^- groups and Zn(II) in the XNBR matrix that consume the free —COOH groups and give rise to new carboxylate-metal interactions [36, 37].

To confirm that the anchored Zn(II) centers in Sep@APTES-Zn are available and participate in the coordination with the carboxyl groups of XNBR, SA was employed as a model molecule bearing —COOH groups, and its interaction with Sep@APTES-Zn was investigated. To this purpose, the filler was mechanically mixed with SA and the thermal events associated to their interaction, as well as the possible formation/evolution of reaction products, were evaluated by DSC analysis. The results are summarized in Figure 6.

When mixed with SA, both bare Sep-OH and Sep@APTES-Zn show an endothermic peak in the heating scan (Figure 6a) associated with the melting of SA at about 65°C–75°C; this crystallizes again in the cooling scan, leading to an exothermic peak at about 70°C (Figure 6b). Only for Sep@APTES-Zn is an additional endothermic peak at 125°C observed in the heating scan, likely related to the melting of the reaction products formed due to the surface interaction between SA and Zn(II) onto the sepiolite surface (Figure 6a). In fact, Zn-based species and SA are reported to interact after SA melting, giving rise to Zn-stearate like structures that could further undergo melting at higher temperatures [38]. This is also associated with an exothermic peak due to its crystallization in the cooling scan detected at 95°C (Figure 6b). It can be deduced that Zn(II) centers are therefore available for interaction with exposed —COOH groups to form metal stearate complexes. Although these results are not related to the real rubber systems, they are consistent with the previous observations on the FTIR spectra of XNBR based NCs, suggesting their role in the curing process of the XNBR matrix along with ZnO.

A direct fallout of the Zn–carboxylate interaction occurring in XNBR NCs after curing is the increase in torque, which is a first indication of the mechanical reinforcement of the polymer matrix. In light of these considerations, the curing process of XNBR/Sep and XNBR/Sep@APTES-Zn NCs was monitored by registering curing curves at 160°C for 120 min (Figure 7). The main parameters of the curing reaction, that is, the torque increase (ΔM), calculated as the difference between the maximum (M_H) and the minimum torque (M_L), as well as the kinetic parameters, such as the time required for the torque to increase by 1 or 2 units above M_L or to reach 90% of the M_H defined as t_{S1}, t_{S2} and t_{90}, respectively, are reported in Table S1. As expected, for all NCs the torque increases during the curing process due to the formation of cross-links in the elastomeric matrix that is responsible for an increase of composites viscosity. According to the previous observations collected on the Zn(II) and ZnO interactions with COOH in XNBR compounds, these results suggest that both commercial ZnO and Sep@APTES-Zn are efficient in promoting the cross-linking process of XNBR. In fact, by substituting ZnO with Sep@APTES-Zn in the XNBR NCs formulation, similar or higher torque values were obtained by keeping constant Zn amounts. Moreover, in all cases the torque is higher than the unfilled XNBR NC and the torque increase is more significant at the highest filler loadings, due to the reinforcing role

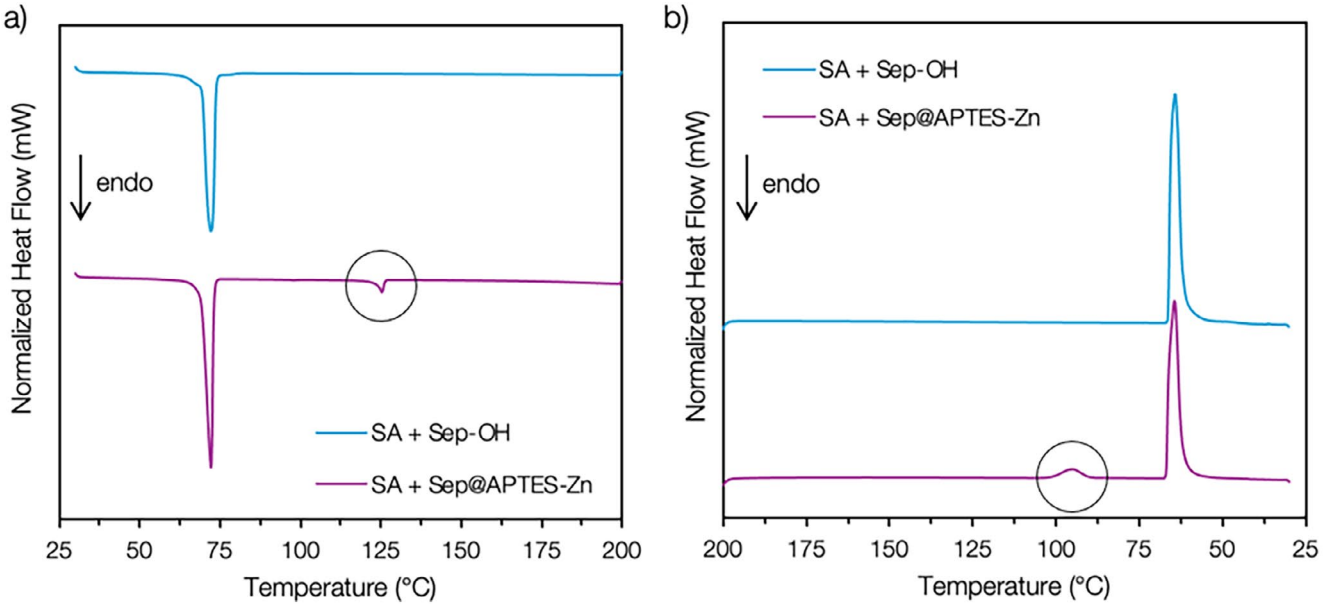

FIGURE 6 | DSC curves of Sep-OH and Sep@APTES-Zn mixed with SA in the temperatures range of: (a) 25°C–200°C (first heating ramp) and (b) 200°C–25°C (first cooling ramp).

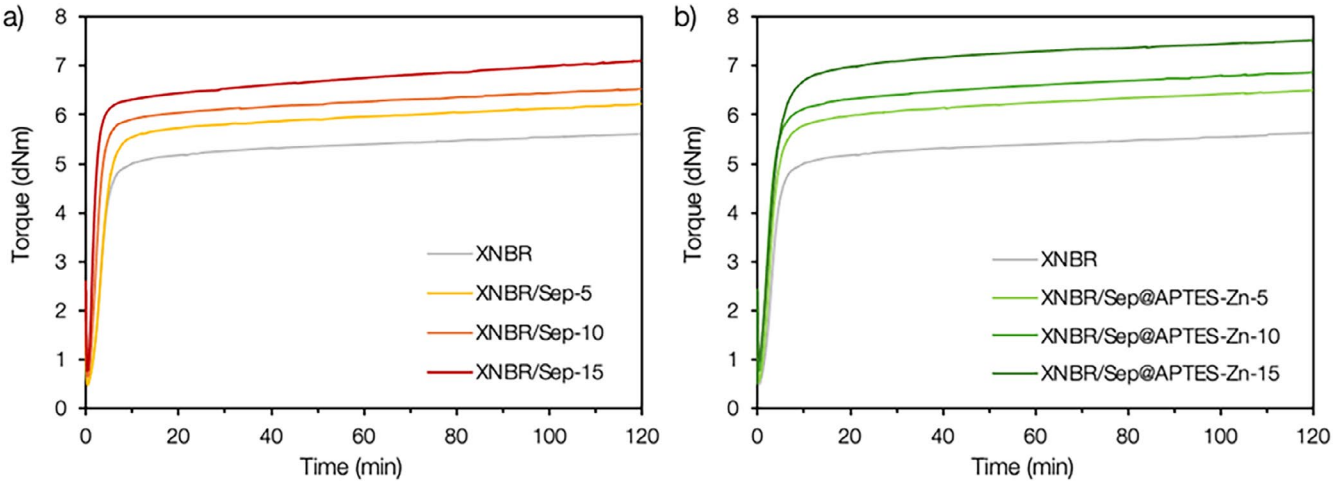

FIGURE 7 | Curing curves of XNBR/Sep-X (a) and XNBR/Sep@APTES-Zn-X (b) compared to the reference XNBR NC.

of the sepiolite filler. Finally, as we previously observed for filled XNBR-Al_2O_3 NCs [22], the constant increase of the torque registered for all NCs even at the end of the curing process, defined as the marching modulus, can be connected to the network reorganization typically observed in ionically cross-linked elastomers [12, 39]. Besides, progressive filler-matrix interactions (mediated by the APTES amino groups) and a progressive reorganization of the filler dispersion may play a role in this torque behavior, independently of the presence of zinc centers onto the surface of the substrate. Thus, the progressive filler dispersion as an additional cause for the marching modulus, presenting this factor together with zinc network reorganization as two potential overlapping factors determining the marching modulus. In terms of reaction kinetics, the presence of Sep@APTES-Zn seems to decrease t_{S1} and t_{S2} by keeping an overall constant t_{90} compared to XNBR NC and to the corresponding XNBR@Sep-X, suggesting that Zn(II) in Sep@APTES-Zn is more available in the first stages of the reaction compared to ZnO. Moreover, these Zn(II) centers keep a good activity during the curing process that is comparable to microcrystalline ZnO used for the reference formulations.

The mechanical behavior of a viscoelastic material is generally described by three parameters: the storage modulus (E′), the loss modulus (E″), and their ratio, the loss factor or tan(δ). Together, these parameters, obtained from DMA, describe the macroscopic dynamic response of the rubber.

Accordingly, the dynamic mechanical properties of XNBR/Sep@APTES-Zn-X NCs were evaluated by DMA (Figure 8). For comparison, the data obtained from a reference compound containing only ZnO (i.e., XNBR/ZnO) are also reported.

In detail, besides a marked decrease in the E′ values observed at approximately 0°C and corresponding to the α relaxation associated with the glass transition temperature (T_g) of XNBR, a second, less pronounced decrease at around 50°C is noticeable

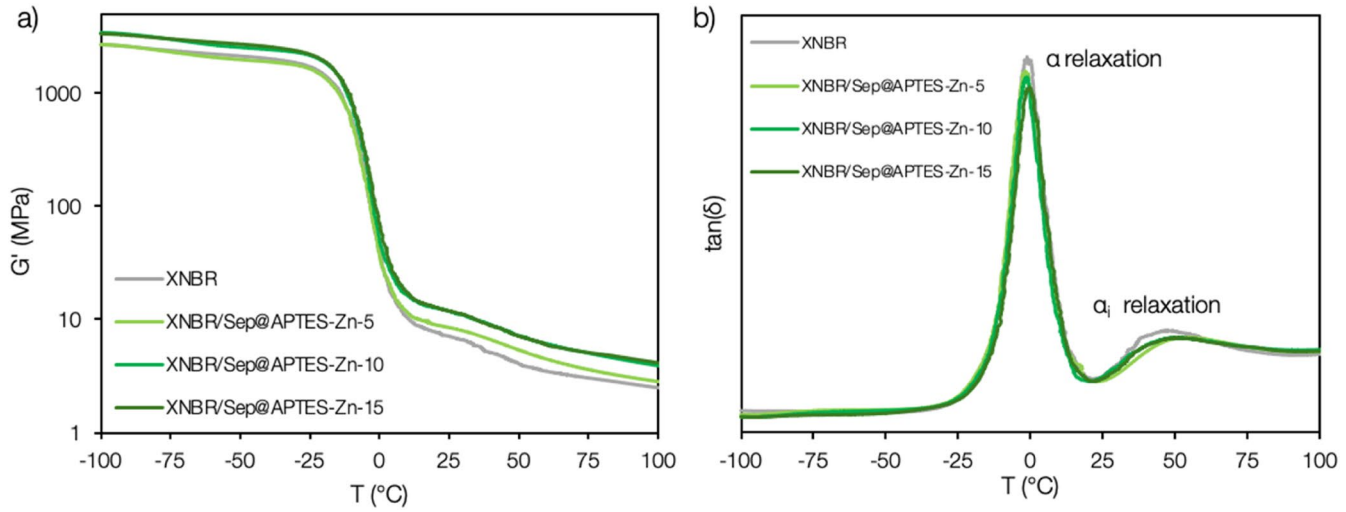

FIGURE 8 | Trend of (a) the storage modulus, G', and (b) tan(δ), as a function of temperature for XNBR/Sep@APTES-Zn-X NCs. The data obtained for the reference XNBR NC (containing only ZnO) are also included for comparison.

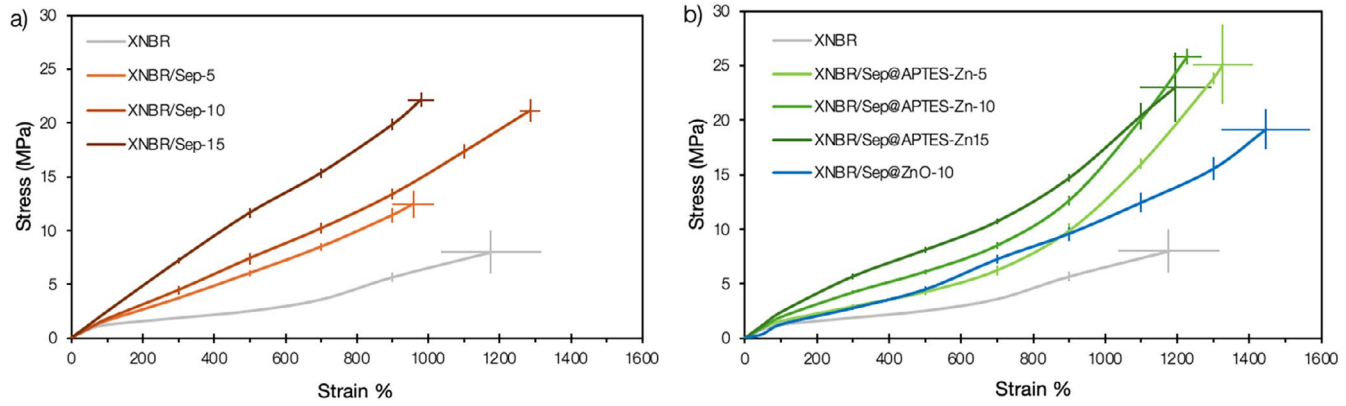

FIGURE 9 | Stress strain curves for (a) XNBR/Sep-X and (b) XNBR/Sep@APTES-Zn-X composites. In (b) the data obtained for the reference composite containing 10 phr of Sep@ZnO are also included for comparison.

(Figure 8a). This is commonly called α_i relaxation (i stands for ionic) and can be related to the transition of the hard phase formed by ionic clusters [36].

Furthermore, at RT, the E′ values increase as the filler concentration rises, becoming almost similar for XNBR/Sep@APTES-Zn-10 and XNBR/Sep@APTES-Zn-15 NCs. This result supports the effect of reinforcement imparted by the filler to the elastomeric matrix.

Also, the two relaxation regions are evident in the tan(δ) curves (Figure 8b). Moreover, with increasing filler loading in XNBR/Sep@APTES-Zn-X NCs, a slight shift of the ionic transition toward higher temperatures is observed compared with the reference XNBR. These results are consistent with the occurrence of additional sites accessible for ionic cluster formation [40].

Finally, to complete the picture of the mechanical properties, stress–strain tests were performed on the NCs. The performances of XNBR/Sep-X and XNBR/Sep@APTES-Zn-X were analyzed and compared to those of XNBR NC and of an additional compound prepared using 10 phr of Sep@ZnO as a filler labeled as XNBR/Sep@ZnO-10. The results are summarized in Figure 9 and Table S2, where the stress at 100% (M100), 300% (M300), and 500% (M500) strain, the values of TS and EB are presented.

Although both fillers enhance mechanical properties, XNBR-Sep-X NCs are generally stiffer (Figure 9a), while XNBR-Sep@APTES-Zn NCs exhibit stress–strain behavior more typical of elastomers and overall superior performance (Figure 9b). In particular, as the loading of Sep and Sep@APTES-Zn fillers increases in the NCs, M100, M300, M500, as well as TS and EB generally show a significant increase (Table S2). These results provide clear evidence of the reinforcing effect of Sep-based fillers on the rubber matrix. Furthermore, when comparing formulations with the same filler loading (10 phr, Figure 9b), Sep@APTES-Zn exhibits slightly superior performance compared to unmodified sepiolite fibers, particularly in terms of TS. This improvement suggests that the surface functionalization of Sep with metal single sites enhances filler–polymer interactions, increasing the availability of Zn(II) species for the formation of ionic crosslinks with the carboxylate groups of XNBR. On the contrary, the absence of any functional groups onto the surface of Sep in XNBR/Sep-X is detrimental in terms of filler-rubber interactions, thus reducing the performance of the NCs at the

breaking point. The trend observed at low strains seems quite different. The influence of filler dispersion on mechanical performance is known to be strain dependent. Recent work by Salamanca et al. [41] demonstrated that the degree of dispersion primarily governs the mechanical response at low extensions, where the filler network structure dominates reinforcement and energy dissipation. This trend is consistent with computational studies, such as the work of Zhang et al. [42], who showed that poorly dispersed fillers amplify interfacial stresses and intensify the Payne effect, phenomena that manifest almost exclusively in the low strain regime.

3.3 | Self-Healing Properties

The self-repairing capability of the NCs was evaluated by comparing the mechanical properties of the repaired samples with those of the pristine ones, which were subjected to the same temperature and pressure conditions used during the healing process. Specifically, the TS and EB values measured before and after the healing procedure were used to calculate the healing efficiency (η). The results are summarized in Figure 10 and Tables S3,S4.

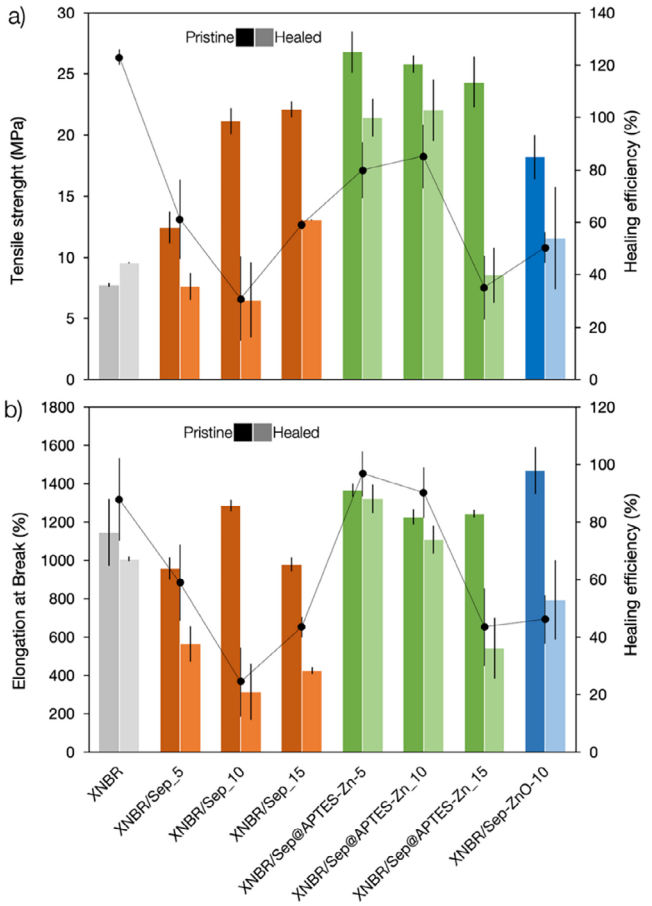

FIGURE 10 | Healing efficiencies (shown with black dots) calculated from (a) TS and (b) EB for XNBR/Sep-X and XNBR/Sep@APTES-Zn-X NCs, according to Equations (1) and (2). The data obtained for the reference composite containing 10 phr of Sep@ZnO are also included for comparison. Left columns (plain color) represent the pristine samples while right columns (light color) represent the healed samples.

In general, the healed samples show lower values of TS and EB. This effect is particularly evident for composites containing unmodified Sep, as well as for XNBR/Sep@ZnO. Interestingly, XNBR/Sep@APTES-Zn-5 and XNBR/Sep@APTES-Zn-10 exhibit a marked recovery of mechanical properties after healing, with healing efficiencies approaching 90% and 100% when calculated from TS and EB, respectively. Moreover, at the same filler loading, the composite containing Sep@APTES-Zn shows a significantly higher healing efficiency than the composite containing Sep@ZnO. These results suggest that isolated Zn centers, though immobilized on the filler surface, interact more effectively with the carboxylate groups of XNBR than ZnO NPs, thereby promoting the formation of thermally reversible interactions. Only in the presence of high loadings of Sep@APTES-Zn (15 wt%) lower TS and EB are measured, possibly ascribed to a non-optimized filler distribution in the NC.

It is also worth noting that the reference sample composed of XNBR and ZnO exhibits high healing efficiency. However, its mechanical properties (Figure 8 and Figure 9) are significantly lower than those of the NCs containing Sep@APTES-Zn.

Overall, the results of the mechanical and functional characterizations indicate that the incorporation of Sep@APTES-Zn represents a good compromise for achieving both improved mechanical performance and effective self-healing behavior. Moreover, anchoring the Zn centers onto the filler surface through covalent interactions with the ligands could help prevent potential metal leaching.

3.4 | NMR Time Domain Results

To elucidate the origin of a good tradeoff between mechanical reinforcement and self-healing behavior observed for Sepiolite decorated with Zn centers, ^{1}H TD-NMR experiments were performed, with the aim of comparing the XNBR polymer chain dynamics in the presence of functionalized Sep fibers (Sep@APTES), Sep@APTES–Zn, and Sep@ZnO. In detail, three *ad-hoc* formulations containing 10 phr of the different fillers and prepared without the addition of a ZnO curing system were analyzed (see Table 1, Section 2).

TD-NMR experiments probe the strength of filler–polymer interactions and the dynamics of polymer chains as reorganized in the presence of the filler. In particular, the relaxation times T_1 and T_2, which describe the recovery of magnetization to the equilibrium state after the radiofrequency pulse, are closely related to the molecular motion regime of the material. While T_1 is generally more suitable for investigating highly localized motions, T_2 (the transverse relaxation time) reflects proton mobility and local molecular environments on a broader scale.

The Hahn Echo (HE) sequence is the most commonly used method to measure the T_2 relaxation time in polymer melts. Differences in polymer chain mobility can be derived from the fitting of HE decay curves. For liquids or systems with high mobility and good homogeneity, the decay can be fitted with a simple exponential function. Conversely, in inhomogeneous systems characterized by different degrees of mobility (e.g., regions with local constraints or freely rotating chains), the mobile fraction can be described by multiple exponential decays. In highly constrained phases, such

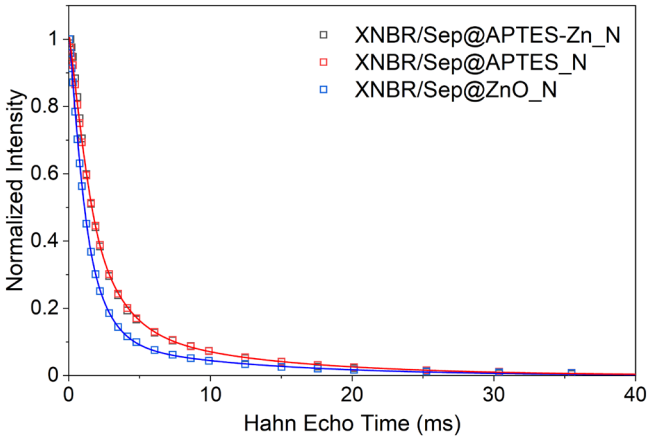

FIGURE 11 | T_2 trends and three-component exponential function of XNBR/Sep@APTES_N, XNBR/Sep@APTES-Zn_N, and XNBR/Sep@ZnO_N.

as vulcanized rubber, a Gaussian decay is typically observed. In crystalline or glassy phases, strong dipolar coupling leads to very rapid signal decay. HE experiments are effective for describing the proton population with enhanced mobility, whereas they are not suitable for accurately mapping the rigid fraction, which is instead quantified using the MSE sequence. Figure 11 shows the HE decay curves at RT for XNBR/Sep@APTES_N, XNBR/Sep@APTES-Zn-10_N and XNBR/Sep@ZnO-10_N. For all samples, the relaxation behavior was satisfactorily fitted using a three-component decay function (see Equation S5 and Table S5), indicating the presence of three distinct proton populations: a highly constrained fraction (A), a slightly constrained fraction (B), and a mobile one (C). These can be associated with highly crosslinked regions, regions with intermediate crosslinking, and non- crosslinked regions, respectively. Looking at the individual systems, the incorporation of Sep@ZnO into the XNBR matrix (XNBR/Sep@ZnO_N) results in a shorter T_2b value and higher B fraction. This suggests the formation of a significant portion of polymer domains with intermediate mobility across the entire rubber matrix and the occurrence of a homogeneous cross-link density, that is likely connected to the good dispersion of ZnO within the matrix. This quantitative behavior finds an immediate visual correspondence in the T_2 relaxation trends (Figure 11) where the curve of XNBR/Sep@ZnO_N composite clearly stands out, showing a distinctly different profile compared to the others.

In contrast, the use of Sep@APTES leads to an increase in T_2b, accompanied by a decrease in B and an increase in C fractions. These variations suggest that in the absence of a zinc source, as in the case of XNBR/Sep@APTES_N, a reduced cross-linking occurs, resulting in a higher fraction of mobile chains within the matrix. This is in full agreement with the well-established role of Zn in promoting the cross-linking within XNBR composites. More interestingly, the use of Sep@APTES-Zn is associated with a significant increase in the A fraction compared to the other two composites. This suggests the formation of an interfacial region characterized by restricted chain mobility around the sepiolite filler that likely promotes an increase of the stiffness of the rigid fraction while reducing the degrees of freedom of the more mobile chains. This provides strong evidence that Zn(II) ions are firmly bound onto the Sep surface and play an active role in coordinating with XNBR chains. Visually, this modification does not lead to an immediately obvious shift in the main relaxation region of the XNBR/Sep@APTES-Zn_N curve compared to its zinc-free counterpart. In fact, as this phenomenon specifically involves population A (the rigid fraction), the variation is localized at the very beginning of the curve and leaves the long-term visual trend unaltered.

In parallel, population C for this composite is again higher compared to XNBR/Sep@ZnO_N, suggesting the presence of a highly mobile fraction, similar to what was detected for XNBR/Sep@APTES_N. This indicates a more heterogeneous distribution of chain dynamics within the network. Such mobility heterogeneity is likely responsible for the synergistic balance between enhanced tensile performance and the effective self-healing capability observed in these systems. Indeed, the coexistence of relatively constrained domains, which contribute to mechanical reinforcement, and more mobile regions, which facilitate chain rearrangement and interdiffusion, is expected to promote efficient healing while maintaining satisfactory mechanical integrity.

4 | Conclusions

This study presents the successful development of naturally occurring sepiolite-based fillers functionalized with APTES and Zn(II) centers (Sep@APTES-Zn), achieving efficient surface modification while preserving a homogeneous distribution of coordinated Zn sites. These metal centers, anchored through amine functionalities, act as readily accessible interaction points for XNBR polymer chains, enabling the formation of dynamic and potentially thermoreversible interactions within the material.

Once incorporated into the XNBR matrix, Sep@APTES-Zn behaves as a multifunctional filler, combining a reinforcing effect with the ability to promote ionic crosslinking via Zn–carboxylate interactions, as demonstrated by FTIR and DSC. This dual role translates into composites with enhanced mechanical performance compared to both unmodified sepiolite and conventional ZnO-based systems, while retaining desirable elastomeric properties. Curing and spectroscopic analyses further highlight the high reactivity and availability of the anchored Zn(II) species, particularly in the early stages of network formation.

A key outcome is self-healing behavior achieved at intermediate filler loadings (5–10 phr), where healing efficiencies of Sep@APTES-Zn approach 100% in EB and ~90% in TS. These performances significantly overtake those of reference ZnO-filled composites (i.e., XNBR/Sep-ZnO), emphasizing the superior effectiveness of isolated Zn centers in enabling dynamic and reversible interactions within the network.

Time-domain NMR results provide further insight into the structure–property relationships, revealing that Sep@APTES-Zn induces a heterogeneous network characterized by the coexistence of constrained and moderately mobile polymer domains. This balance in chain dynamics appears crucial: rigid regions contribute to mechanical reinforcement, while mobile segments enable chain rearrangement and interdiffusion, thus facilitating efficient self-healing.

Overall, the strategy of anchoring Zn(II) centers onto sepiolite through covalent functionalization represents an effective

approach to design advanced elastomer NCs with an optimal combination of mechanical strength and self-repair capability, while also mitigating potential issues related to Zn leaching.

Author Contributions

Silvia Mostoni: conceptualization, writing – original draft, writing – review and editing, visualization, methodology, data curation, supervision, investigation, formal analysis. **Marianella Hernandez Santana:** conceptualization, writing – review and editing, validation, methodology, resources, supervision, formal analysis, project administration. **Itziar Mas Giner:** investigation, writing – review and editing, methodology, validation, visualization. **Michele Mauri:** investigation, writing – review and editing, methodology, validation, visualization, data curation, formal analysis. **Paolo Valagussa:** investigation, writing – original draft, writing – review and editing, formal analysis, data curation, validation, visualization, methodology. **Roberto Simonutti:** methodology, visualization, writing – review and editing, data curation, resources, formal analysis. **Emanuela Callone:** investigation, writing – review and editing, validation, methodology, visualization, data curation, formal analysis. **Sandra Diré:** writing – review and editing, visualization, validation, methodology, supervision, formal analysis, conceptualization. **Barbara Di Credico:** writing – review and editing, methodology, resources, visualization, formal analysis. **Roberto Scotti:** methodology, visualization, writing – review and editing, resources, formal analysis. **Massimiliano D'Arienzo:** conceptualization, writing – original draft, writing – review and editing, funding acquisition, project administration, resources, supervision, validation, methodology, visualization, formal analysis.

Acknowledgments

Authors thank Dr. Marta Colombo and Dr. Sofia Faina for their contribution to the experimental work related to the characterization of polymer composites, and Francesco Travaglini for the TD-NMR measurements. Open access publishing facilitated by Universita degli Studi di Milano-Bicocca, as part of the Wiley - CRUI-CARE agreement.

Conflicts of Interest

The authors declare no conflicts of interest.

Data Availability Statement

The data that support the findings of this study are available from the corresponding author upon reasonable request.

References

1. P. Sahu, J. S. Oh, and A. I. Isayev, "Recycling and Circular Economy of Thermoplastic Elastomers," in *Advances in Thermoplastic Elastomers: Challenges and Opportunities* (Elsevier, 2024), 529–561, https://doi.org/10.1016/B978-0-323-91758-2.00009-X.

2. A. Fazli and D. Rodrigue, "Waste Rubber Recycling: A Review on the Evolution and Properties of Thermoplastic Elastomers," *Materials* 13, no. 3 (2020): 782, https://doi.org/10.3390/ma13030782.

3. R. P. Wool, "Self-Healing Materials: A Review," *Soft Matter* 4, no. 3 (2008): 400, https://doi.org/10.1039/b711716g.

4. M. A. Sattar and A. Patnaik, "Design Principles of Interfacial Dynamic Bonds in Self-Healing Materials: What Are the Parameters?," *Chemistry, an Asian Journal* 15, no. 24 (2020): 4215–4240, https://doi.org/10.1002/asia.202001157.

5. M. Nakahata, Y. Takashima, H. Yamaguchi, and A. Harada, "Redox-Responsive Self-Healing Materials Formed From Host–Guest Polymers," *Nature Communications* 2, no. 1 (2011): 511, https://doi.org/10.1038/ncomms1521.

6. Y. Shi, M. Wang, C. Ma, Y. Wang, X. Li, and G. Yu, "A Conductive Self-Healing Hybrid Gel Enabled by Metal–Ligand Supramolecule and Nanostructured Conductive Polymer," *Nano Letters* 15, no. 9 (2015): 6276–6281, https://doi.org/10.1021/acs.nanolett.5b03069.

7. N. F. Mohd Sani, H. J. Yee, N. Othman, A. A. Talib, and R. K. Shuib, "Intrinsic Self-Healing Rubber: A Review and Perspective of Material and Reinforcement," *Polymer Testing* 111 (2022): 107598, https://doi.org/10.1016/j.polymertesting.2022.107598.

8. N. F. Mohd Sani, N. A. Majid, A. Rehman, et al., "A Review of the Recent Development in Self-Healing Rubbers and Their Quantification Methods," *Progress in Rubber, Plastics and Recycling Technology* 40, no. 2 (2024): 203–241, https://doi.org/10.1177/14777606231200952.

9. A. Eisenberg, J.-S. Kim, and M. Ratner, "Introduction to Ionomers," *Physics Today* 52, no. 2 (1999): 68, https://doi.org/10.1063/1.882601.

10. N. Hohlbein, A. Shaaban, A. R. Bras, W. Pyckhout-Hintzen, and A. M. Schmidt, "Self-Healing Dynamic Bond-Based Rubbers: Understanding the Mechanisms in Ionomeric Elastomer Model Systems," *Physical Chemistry Chemical Physics* 17, no. 32 (2015): 21005–21017, https://doi.org/10.1039/C5CP00620A.

11. L. Leibler, M. Rubinstein, and R. H. Colby, "Dynamics of Reversible Networks," *Macromolecules* 24, no. 16 (1991): 4701–4707, https://doi.org/10.1021/ma00016a034.

12. S. Utrera-Barrios, J. Araujo-Morera, L. Pulido de Los Reyes, et al., "An Effective and Sustainable Approach for Achieving Self-Healing in Nitrile Rubber," *European Polymer Journal* 139 (2020): 110032, https://doi.org/10.1016/j.eurpolymj.2020.110032.

13. B. Kim, S. Kim, R. Kim, et al., "Comparative Toxicity of Tire Wear Particle Leachates: Zinc as a Key Toxicant Affecting Development and Motility in Zebrafish Larvae," *Journal of Hazardous Materials* 499 (2025): 140296, https://doi.org/10.1016/j.jhazmat.2025.140296.

14. Z. A. Ganie, S. Guchhait, M. Talib, A. Choudhary, and G. K. Darbha, "Investigating the Sorption of Zinc-Oxide Nanoparticles on Tire-Wear Particles and Their Toxic Effects on *Chlorella vulgaris*: Insights From Toxicological Models and Physiological Analysis," *Journal of Hazardous Materials* 483 (2025): 136648, https://doi.org/10.1016/j.jhazmat.2024.136648.

15. S. Mostoni, P. Milana, B. Di Credico, M. D'Arienzo, and R. Scotti, "Zinc-Based Curing Activators: New Trends for Reducing Zinc Content in Rubber Vulcanization Process," *Catalysts* 9, no. 8 (2019): 664, https://doi.org/10.3390/catal9080664.

16. S. Mostoni, M. D'Arienzo, B. di Credico, et al., "Design of a Zn Single-Site Curing Activator for a More Sustainable Sulfur Cross-Link Formation in Rubber," *Industrial and Engineering Chemistry Research* 60, no. 28 (2021): 10180–10192, https://doi.org/10.1021/acs.iecr.1c01580.

17. E. Nadim, I. Major, D. Devine, and P. Paraskar, "Biobased Self-Healing Functional Composites and Their Applications," *Journal of Materials Science: Composites* 6, no. 1 (2025): 3, https://doi.org/10.1186/s42252-025-00065-x.

18. S. Mostoni, P. Milana, C. Marano, et al., "Localizing the Cross-Links Distribution in Elastomeric Composites by Tailoring the Morphology of the Curing Activator," *Composites Science and Technology* 230 (2022): 109780, https://doi.org/10.1016/j.compscitech.2022.109780.

19. G. Zhang, C. Tian, J. Shi, et al., "Mechanically Robust, Self-Repairable, Shape Memory and Recyclable Ionomeric Elastomer Composites With Renewable Lignin via Interfacial Metal–Ligand Interactions," *ACS Applied Materials & Interfaces* 14, no. 33 (2022): 38216–38227, https://doi.org/10.1021/acsami.2c10731.

20. J. X. Jiang, X. Y. Jia, D. Y. Zhu, et al., "Regulation of Lignin Microstructures to Construct Fully Biomass-Based Elastomers for Large Crack Self-Healing Artificial Muscles," *Small* 21, no. 22 (2025): e2412557, https://doi.org/10.1002/smll.202412557.

21. S. Utrera-Barrios, O. Ricciardi, S. González, R. Verdejo, M. Á. López-Manchado, and M. Hernández Santana, "Development of Sustainable, Mechanically Strong, and Self-Healing Bio-Thermoplastic Elastomers Reinforced With Alginates," *Polymers* 14, no. 21 (2022): 4607, https://doi.org/10.3390/polym14214607.

22. S. Faina, M. Colombo, L. Mirizzi, et al., "Al2O3 Decorated With Zn Single Sites: A Multifunctional Filler for Upgrading the Properties of XNBR Composites," *ACS Applied Polymer Materials* 7, no. 1 (2025): 234–246, https://doi.org/10.1021/acsapm.4c02946.

23. W. J. Miles, "Amargosa Sepiolite and Saponite: Geology, Mineralogy, and Markets," in *Developments in Clay Science* vol. 3 (Elsevier, 2011), 265–277, https://doi.org/10.1016/B978-0-444-53607-5.00011-6.

24. B. Di Credico, E. Cobani, E. Callone, et al., "Size-Controlled Self-Assembly of Anisotropic Sepiolite Fibers in Rubber Nanocomposites," *Applied Clay Science* 152 (2018): 51–64, https://doi.org/10.1016/j.clay.2017.10.032.

25. I. Tagliaro, E. Cobani, E. Carignani, et al., "The Self-Assembly of Sepiolite and Silica Fillers for Advanced Rubber Materials: The Role of Collaborative Filler Network," *Applied Clay Science* 218 (2022): 106383, https://doi.org/10.1016/j.clay.2021.106383.

26. S. Utrera-Barrios, N. Steenackers, S. Terryn, et al., "Unlocking the Potential of Self-Healing and Recyclable Ionic Elastomers for Soft Robotics Applications," *Materials Horizons* 11, no. 3 (2024): 708–725, https://doi.org/10.1039/D3MH01312J.

27. M. Calovi, E. Callone, R. Ceccato, F. Deflorian, S. Rossi, and S. Dirè, "Effect of the Organic Functional Group on the Grafting Ability of Trialkoxysilanes Onto Graphene Oxide: A Combined NMR, XRD, and ESR Study," *Materials* 12, no. 23 (2019): 3828, https://doi.org/10.3390/ma12233828.

28. G. S. Caravajal, D. E. Leyden, G. R. Quinting, and G. E. Maciel, "Structural Characterization of (3-Aminopropyl)triethoxysilane-Modified Silicas by Silicon-29 and Carbon-13 Nuclear Magnetic Resonance," *Analytical Chemistry* 60, no. 17 (1988): 1776–1786, https://doi.org/10.1021/ac00168a027.

29. S. Maeda, S. Oumae, S. Kaneko, and K.-K. Kunimoto, "Formation of Carbamates and Cross-Linking of Microbial Poly(ε-l-Lysine) Studied by 13C and 15N Solid-State NMR," *Polymer Bulletin* 68, no. 3 (2012): 745–754, https://doi.org/10.1007/s00289-011-0580-2.

30. D. Bugnotti, S. Dalle Vacche, L. H. Esposito, et al., "Structure of Starch–Sepiolite Bio-Nanocomposites: Effect of Processing and Matrix–Filler Interactions," *Polymers* 15, no. 5 (2023): 1207, https://doi.org/10.3390/polym15051207.

31. M. R. Weir, W. Kuang, G. A. Facey, and C. Detellier, "Solid-State Nuclear Magnetic Resonance Study of Sepiolite and Partially Dehydrated Sepiolite," *Clays and Clay Minerals* 50, no. 2 (2002): 240–247, https://doi.org/10.1346/000986002760832838.

32. P. R. Reddy, M. Radhika, and P. Manjula, "Synthesis and Characterization of Mixed Ligand Complexes of Zn(II) and co(II) With Amino Acids: Relevance to Zinc Binding Sites in Zinc Fingers," *Journal of Chemical Sciences* 117, no. 3 (2005): 239–246, https://doi.org/10.1007/BF02709293.

33. J. Peisach and W. E. Blumberg, "Structural Implications Derived From the Analysis of Electron Paramagnetic Resonance Spectra of Natural and Artificial Copper Proteins," *Archives of Biochemistry and Biophysics* 165, no. 2 (1974): 691–708, https://doi.org/10.1016/0003-9861(74)90298-7.

34. C. C. R. Sutton, G. da Silva, and G. V. Franks, "Modeling the IR Spectra of Aqueous Metal Carboxylate Complexes: Correlation Between Bonding Geometry and Stretching Mode Wavenumber Shifts," *Chemistry—a European Journal* 21, no. 18 (2015): 6801–6805, https://doi.org/10.1002/chem.201406516.

35. G. Deacon, "Relationships Between the Carbon-Oxygen Stretching Frequencies of Carboxylato Complexes and the Type of Carboxylate Coordination," *Coordination Chemistry Reviews* 33, no. 3 (1980): 227–250, https://doi.org/10.1016/S0010-8545(00)80455-5.

36. A. Laskowska, M. Zaborski, G. Boiteux, O. Gain, A. Marzec, and W. Maniukiewicz, "Ionic Elastomers Based on Carboxylated Nitrile Rubber (XNBR) and Magnesium Aluminum Layered Double Hydroxide (Hydrotalcite)," *Express Polymer Letters* 8, no. 6 (2014): 374–386, https://doi.org/10.3144/expresspolymlett.2014.42.

37. U. Mandal, "Ionic Elastomer Based on Carboxylated Nitrile Rubber: Infrared Spectral Analysis," *Polymer International* 49, no. 12 (2000): 1653–1657, https://doi.org/10.1002/1097-0126(200012)49:12<1653::AID-PI586>3.0.CO;2-U.

38. F. W. H. Kruger and W. J. McGill, "A DSC Study of Curative Interactions. I. The Interaction of ZnO, Sulfur, and Stearic Acid," *Journal of Applied Polymer Science* 42, no. 10 (1991): 2643–2649, https://doi.org/10.1002/app.1991.070421002.

39. S. Utrera-Barrios, R. Verdugo Manzanares, J. Araujo-Morera, et al., "Understanding the Molecular Dynamics of Dual Crosslinked Networks by Dielectric Spectroscopy," *Polymers (Basel)* 13, no. 19 (2021): 3234, https://doi.org/10.3390/polym13193234.

40. S. Utrera-Barrios, M. F. Martínez, I. Mas-Giner, R. Verdejo, M. A. López-Manchado, and M. Hernández Santana, "New Recyclable and Self-Healing Elastomer Composites Using Waste From Toner Cartridges," *Composites Science and Technology* 244 (2023): 110292, https://doi.org/10.1016/j.compscitech.2023.110292.

41. F. M. Salamanca, M. Narvaez-Fagoaga, M. Montero-Escrivá, Z. Zepeda-Rodríguez, L. B. Tunnicliffe, and J. L. Valentin, "Investigating Filler-Rubber Interactions and Amplification Effect in Reinforced Elastomers," *Polymer (Guildford)* 360 (2026): 130367, https://doi.org/10.1016/j.polymer.2026.130367.

42. M. Viktorova, R. Hentschke, F. Fleck, F. Taherian, and H. A. Karimi-Varzaneh, "Simulation of Elastomer Nanocomposites: Interfacial Stresses and Strains Related to Filler Dispersion, Global Deformation and the Payne Effect," *Computational Materials Science* 223 (2023): 112144, https://doi.org/10.1016/j.commatsci.2023.112144.

Supporting Information

Additional supporting information can be found online in the Supporting Information section. **Figure S1:** XRD patterns of Sep@APTES-Zn compared to bare Sep-OH. **Figure S2:** Nitrogen physisorption isotherms at 77 K for (a) Sep-OH, (b) Sep@APTES and (c) Sep@APTES-Zn. **Figure S3:** ATR/FTIR spectra of APTES and Zn(NO3)2 precursors. **Figure S4:** 29Si CPMAS NMR spectra of Sep-OH and functionalized Sep samples. **Figure S5:** SEM micrographs of Sep@APTES-Zn at different magnifications. **Figure S6:** EPR spectrum of Sep@APTES-Zn/Cu prepared by substituting Zn(II) with Cu(II) (0.01%); the inset shows the Peisach–Blumberg correlation diagram for oxygen and nitrogen coordinating Cu(II) ions. **Figure S7:** TGA curves of (a) XNBR/Sep-X and (b) XNBR/Sep@APTES-Zn-X NCs. In both graphs the gray curve is the reference XNBR NC prepared by using ZnO as reported in Table 1 of the main text. **Table S1:** Parameters of the curing curves registered for XNBR/Sep-X, XNBR/Sep@APTES-ZnX and XNBR NCs. In the first three colums the kinetic parameters are reported: tS1, tS2 and tS90 represent the time required to achieve 1%, 2% or 90% of the maximum torque. In the latter three columns the torque increase (ΔM), calculated as the difference between the maximum (MH) and the minimum torque (ML) are also shown. **Table S2:** Parameter of the tensile tests performed on XNBR/Sep-X, XNBR/Sep@APTES-Zn-X compared to XNBR and XNBR/Sep@ZnO-10. In the Table the values of the measured stress at 100% (M100), 300% (M300) and 500% (M500) strain, along with the values of tensile strength (TS) and elongation at break (EB) are reported. **Table S3:** Healing efficiency (η, %) calculated from TS values of the healed and pristine NCs, according to Equation 1 of the main text. **Table S4:** Healing efficiency (η, %) calculated from EB values of the healed and pristine NCs, according to Equation 1 of the main text. **Table S5:** Exponential function parameters of XNBR/Sep@APTES_N, XNBR/Sep@APTES-Zn-10_N and XNBR/Sep@ZnO-10_N NCs, according to Equations 5.